Eurographics Conference on Visualization (EuroVis) 2015
H. Carr, K.-L. Ma, and G. Santucci
(Guest Editors)

Volume 34 (2015), Number 3

Finite-Time Mass Separation for Comparative Visualizations of Inertial Particles

Tobias Günther and Holger Theisel

Visual Computing Group, University of Magdeburg

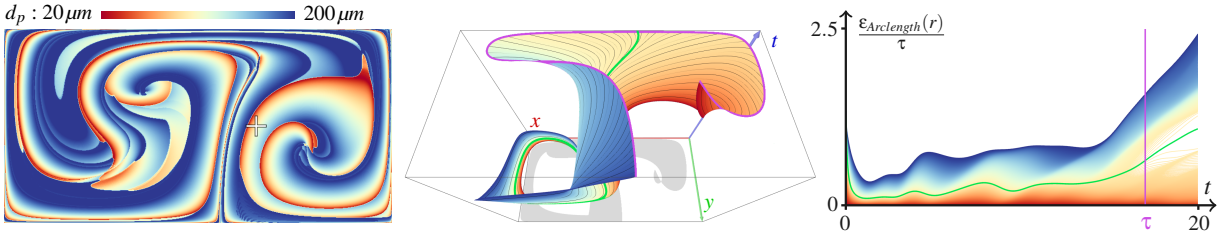

Figure 1: Mass separation of inertial particles in the DOUBLE GYRE. Left image: Mass (color-coded) that separates strongest during integration over time $\tau = 17$. Center image: inertial particles of different mass are released at the cross in the left image. In space-time their trajectories assemble a surface, with the purple line being its frontline—a so-called massline. The green line is the particle trajectory with strongest separation (here, with diameter $d_p = 99\,\mu m$). Right image: plot of difference to reference particle, here the smallest inertial particle (diameter $d_p = 20\,\mu m$), which makes the temporal evolution of the separation apparent.

Abstract

The visual analysis of flows with inertial particle trajectories is a challenging problem because time-dependent particle trajectories additionally depend on mass, which gives rise to an infinite number of possible trajectories passing through every point in space-time. This paper presents an approach to a comparative visualization of the inertial particles' separation behavior. For this, we define the Finite-Time Mass Separation (FTMS), a scalar field that measures at each point in the domain how quickly inertial particles separate that were released from the same location but with slightly different mass. Extracting and visualizing the mass that induces the largest separation provides a simplified view on the critical masses. By using complementary coordinated views, we additionally visualize corresponding inertial particle trajectories in space-time by integral curves and surfaces. For a quantitative analysis, we plot Euclidean and arc length-based distances to a reference particle over time, which allows to observe the temporal evolution of separation events. We demonstrate our approach on a number of analytic and one real-world unsteady 2D field.

1. Introduction

The study of inertial particles is an emerging field in flow visualization. While traditional flow visualization aims for insights on the dynamics of the flow itself, inertial particles are observed to understand the behavior of finite-sized objects moving therein. This has numerous applications, for instance in sand saltation modeling [SL99], soiling of cars [RSBE01], visual obscuration in helicopter landing maneuvers [KGRK14], formation of rain [Bor11] or even in jellyfish feeding [PD09]. Among the many unresolved problems that center around inertial particles is the search for an effective visualization of the differences between inertial particle trajectories, for instance to locate regions in which massless trajectories are similar enough to fall back on stan-

dard techniques. In the context of this paper, comparative visualization comprises both the qualitative and quantitative comparison with reference particles, as well as the detection of critical masses that cause a separation of differently sized inertial particles. The latter plays a major role in rotorcraft engineering [SGL10], as sand particles dragged into a rotor disk cause mechanical wear and entrain further particles when being convected to the sediment bed, which severely hinders the pilot's view. For quantitative comparisons, common practice is to plot the Euclidean distance between differently sized inertial particles over time [Bor11], which however, suffers from occlusion and is unaware of the behavior of particle sizes in-between. Up until now, it was not possible to effectively explore where mass separation occurs, how distinct it is and which masses are separating. The difficulty of quantifying trajectory differences and the integration-based nature of separation detection make these problems challenging.

In this paper, we introduce *Finite-Time Mass Separation* (FTMS). Inspired by the inertial extension [SH09, PD09] of FTLE [Hal01, SLM05], the idea is to release inertial particles from the same location, but with slightly varied mass and to observe their separation behavior over time. Inertial FTLE, on the other hand, observes the separation due to spatial variation of the seed point, which can lead to different answers. Locating the mass that produces the *largest separation* in FTMS allows to extract and visualize critical masses. In addition, we complement the visualization by two coordinated views that provide detailed information on the mass-dependent particle trajectories released at a given seed point. In a *plot view*, we use a new distance measure between inertial particle trajectories that is occlusion-free and considers the actions of particles in-between. This view allows to quantitatively measure absolute and relative differences, provides insights on how separation evolves over time and allows to quickly locate separation events. In a *domain view*, we depict inertial particle trajectories of unsteady 2D flows in 3D space-time, which embeds the trajectories in the domain and allows to see how they separate. By varying the mass, inertial particle trajectories assemble a surface, on which separation can be shown by visualizing its stretching.

This paper contributes a novel measure for mass separation, called FTMS, and its comparison to inertial FTLE [SH09, PD09]. Moreover, it enables quantitative measurements with a new difference metric that avoids cluttering and a comparison with Euclidean distances, as well as a spatial embedding of the separation on a surface in the space-time domain. With this, we provide the first comprehensive study of the mass-dependent behavior of inertial particles that answers: *where* and *when* mass separation occurs, *which* masses are separating and *what* the separation looks like in the domain.

2. Background and Related Work

The following section lays the foundation by introducing into the modeling of inertial particles and the abstraction from the underlying equations of motion using the concept of a mass-dependent flow map. Afterwards, we discuss related work on visualizations in the field of inertial particles.

2.1. Modeling of Inertial Particles

The trajectories of inertial particles are determined by their underlying equations of motion. Typically, they involve a number of forces that act on the particles, such as the force exerted by the flow itself, buoyancy, Stokes drag, the force exerted due to the mass of the fluid moving with the particle and the Basset-Boussinesq memory term, cf. Haller and Sapsis [HS08]. Today's most accepted form of these forces was described by Maxey and Riley [MR83] for small rigid spherical particles. The properties of the solutions to their equations of motion and the history of its corrections were recently documented by Farazmand and Haller [FH15].

Depending on the application, several assumptions can be made that simplify the equations of motion considerably. It is important to note that the visualization concepts introduced in this paper are independent of the chosen equations of motion. For the examples given throughout the paper, we assume particles to be spherical and very small in size, which allows to assume Stokes flow due to the small particle Reynolds number. Also, the particle density is assumed to be far higher than the density of the surrounding fluid, which allows to neglect buoyancy. Further assuming dilute flow, the particle motion is dominated by drag forces, rather than particle-particle collision. Thus, we neglect collision handling and assume one-way coupling, i.e., particles do not affect the surrounding fluid. These simplifications are common and were used for instance in [SGL10, PSGC11a, KGRK14, GT14, CGP*10, BBC*09, BBC*11]. According to Crowe et al. [CST98], they lead to the following equations of motion:

$$\frac{\mathrm{d}\mathbf{x}}{\mathrm{d}t} = \mathbf{v}(t) \qquad \text{with} \quad \mathbf{x}(0) = \mathbf{x}_0 \tag{1}$$

$$\frac{\mathrm{d}\mathbf{v}}{\mathrm{d}t} = \frac{\mathbf{u}(\mathbf{x}(t),t) - \mathbf{v}(t)}{r} + \mathbf{g} \qquad \text{with} \quad \mathbf{v}(0) = \mathbf{v}_0 \tag{2}$$

where $\mathbf{u}(\mathbf{x},t)$ is a time-dependent flow field, $\mathbf{v}$ is the current particle velocity, $\mathbf{g}$ is an (optional) gravity vector, $\mathbf{x}_0$ and $\mathbf{v}_0$ are the initial particle position and velocity, and r is the particle response time. The response time r is characterized by the diameter d_p and density ρ_p of the particle, as well as the viscosity μ of the surrounding fluid:

$$r = \frac{d_p^2 \rho_p}{18\mu} \tag{3}$$

Figuratively spoken, the response time is the time required for a particle released from rest in a gravity-free environment to acquire 63% of the velocity of the carrying fluid, cf. [CST98]. For all examples in the paper, we used as particle density ρ_p the density of dry sand, i.e., $\rho_p = 1600 kg/m^3$. Gravity was set to $\mathbf{g} = \mathbf{0}$. The diameter d_p varies between $d_p = 10\mu m$ and $d_p = 500\mu m$. Note that these equations of motion hold for $d_p \ll \eta_k$, with η_k being the Kolmogorov length scale. The

surrounding medium was assumed to be air, thus the viscosity was set to $\mu = 1.532 \cdot 10^{-5}\, kg/(m \cdot s)$. In the following, we speak at times of mass and particle diameter, rather than referring to the more general response time, since mass and diameter are more accessible. All three directly relate to each other, since density and viscosity are kept constant.

The equations of motion (1) and (2) can be rendered autonomous by making particle position $\mathbf{x}$, particle velocity $\mathbf{v}$ and time t state variables:

$$\frac{\mathrm{d}}{\mathrm{d}t}\begin{pmatrix}\mathbf{x}\\ \mathbf{v}\\ t\end{pmatrix} = \begin{pmatrix}\mathbf{v}\\ \frac{\mathbf{u}(\mathbf{x},t)-\mathbf{v}}{r}+\mathbf{g}\\ 1\end{pmatrix} \quad \text{with} \quad \begin{pmatrix}\mathbf{x}\\ \mathbf{v}\\ t\end{pmatrix}(0) = \begin{pmatrix}\mathbf{x}_0\\ \mathbf{v}_0\\ t_0\end{pmatrix} \tag{4}$$

Viewing the problem in phase space, the state variables on the left hand side are the attributes stored per particle, i.e., position $\mathbf{x}$, velocity $\mathbf{v}$ and time t. Trajectories of inertial particles appear as phase lines, which are in fact tangent curves of the higher-dimensional vector field on the right hand side. More details on the numerical integration [HS08] and an application of this vector field was given in [GT14]. Alternative approaches include the modeling of gravity and buoyancy as external forces by the material derivative, cf. [BBC*09].

A recent report on experimental and computational fluid dynamics of inertial particles in turbulent fluids was compiled by Balachandar and Eaton [BE10]. Of interest in the inertial fluid dynamics literature are problems such as direct numerical simulations of jets [PSGC11a], stirring of sand during helicopter maneuvers [SGL10], comparisons between experimentally determined and simulated trajectories [OOG08] (depicted by Euclidean distances over time), energy dissipation along trajectories [BBC*09], or the effects of inertial particles on the underlying flow (two-way coupling) [PSGC11b].

2.2. Mass-dependent Flow Map

To abstract from the underlying equations of motion, Günther et al. [GKKT13] extended the concept of *flow map* ϕ (cf. [Hal01,SLM05]) to inertial particles. They defined a mass-dependent flow map $\phi_t^\tau(\mathbf{x}, r, \mathbf{v}_0)$ as a function that describes where an inertial particle with response time r, seeded at location $(\mathbf{x},t)$, and with an initial velocity $\mathbf{v}_0$ moves to during integration in flow $\mathbf{u}$ over a time interval τ. This formulation hides the underlying equations of motions, which allows to describe Lagrangian features in a generalized and abstract way. Note that the continuity of the flow map's derivatives depends on the underlying particle model. If random events such as collisions are neglected (as in our case), they are continuous everywhere in the domain. In the following, we consider all particles to be released from rest, i.e., $\mathbf{v}_0 = \mathbf{0}$. For brevity, we therefore shortly denote the mass-dependent flow map for particles released from rest as $\phi_t^\tau(\mathbf{x}, r)$.

2.3. Inertial Particles in Visualization

Integral curves proved to become one of the most important concepts in flow visualization. Using the mass-dependent flow map notation, integral curves have been extended in [GKKT13] for inertial particles. There is one class of integral curves that only arises in the context of inertial particles, which is called *massline*. It is assembled by releasing particles from the same location at the same time, but with *varying mass*. After a certain integration duration particles will drift apart due to inertia. The locations they reach form a curve, which can be expressed as:

$$\mathbf{m}(r) = \phi_t^\tau(\mathbf{x}, r) \tag{5}$$

Masslines are parameterized by the particle mass, which is included in the particle response time r, Eq. (3). They are continuous if the mass partial of the flow map is continuous.

Another important tool that was extended to inertial particles is the extraction of Lagrangian coherent structures (LCS). A repelling LCS is a material structure that repels all particles, whereas an attracting LCS attracts them [Hal01]. These definitions are invariant with respect to the reference frame and therefore objective. Haller [Hal01] has demonstrated that LCS can be extracted as ridges of the finite-time Lyapunov exponent (FTLE) field. A number of variants to LCS calculation have been proposed in the literature, including localized FTLE [KPH*09], a method based on streak surfaces [ÜSE13] and time line cell tracking [KER*14]. An overview can be found in the FTLE benchmark of Kuhn et al. [KRWT12]. Inertial Lagrangian coherent structures (ILCS or pLCS) have been defined in [SH09] and [PD09] as ridges of an FTLE computation based on the trajectories of inertial particles:

$$\mathrm{IFTLE}(\mathbf{x}, t, \tau, r) = \frac{1}{\tau}\ln\sqrt{\lambda_{\max}\left(\frac{\mathrm{d}\phi_t^\tau(\mathbf{x},r)}{\mathrm{d}\mathbf{x}}^{\mathrm{T}}\frac{\mathrm{d}\phi_t^\tau(\mathbf{x},r)}{\mathrm{d}\mathbf{x}}\right)}$$

This scalar field measures the separation of nearby placed, equally-sized particles. Standard FTLE is the special case for massless particles, i.e., $r = 0$. As it turns out, the dynamics of larger inertial particles become instable in areas of high strain [SH08], causing particles to spin away from attracting ILCS due to their inertia rather than being attracted. Both repelling and attracting ILCS have been computed in [SPH11] in the context of jellyfish feeding.

Further work on inertial particles includes the visualization of sand particle density on cars [RSBE01] and the extraction of inertial vortex corelines [GT14].

3. Finite-Time Mass Separation

A so far unaddressed problem in flow visualization is the comparative visualization of inertial particles. This problem is quite challenging, as even from a single point in the domain an infinite number of inertial particles can be released that take different trajectories depending on their mass. Quantifying their differences requires an adequate distance measure and a study of the temporal evolution of these differences. This, however, first of all requires to set a seed point. Unfortunately, it is nearly impossible to predict ad-hoc *when* and

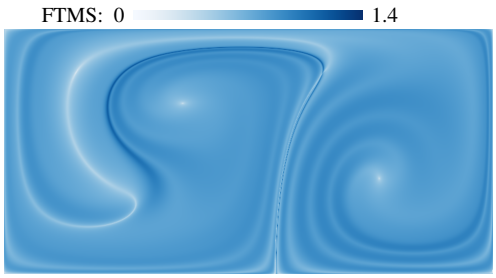

Figure 2: Finite-Time Mass Separation (FTMS) of the DOUBLE GYRE for inertial particles with diameter $d_p = 99\,\mu m$ at $t = 0$ and $\tau = 9.95$.

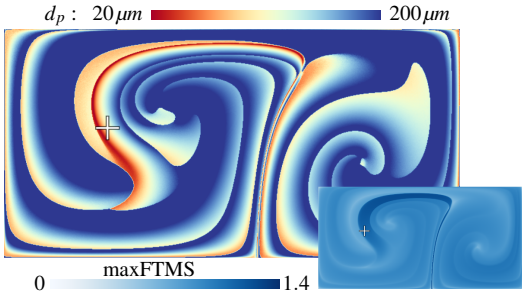

Figure 3: Maximal Finite-Time Mass Separation (maxFTMS) in the DOUBLE GYRE at $t = 0$ after duration $\tau = 9.95$.

where and for *which* mass interesting events occur in the domain. The key to the problem is to analyze the mass-induced separation behavior of inertial particles, as a separation entails the development of a difference. This insight leads us to the definition of the *Finite-Time Mass Separation* (FTMS) field. That is, we strive to quantify at every location in the space-time domain, how quickly inertial particles of slightly different mass separate if they are released from the *same* location. Inertial FTLE, in contrast, describes how inertial particles of the same mass separate if released in proximity, which does not produce insights on the relationship between different masses. Differences to inertial FTLE are discussed later in Section 6.1. FTMS is computed by considering the derivative of the flow map with respect to response time r, which is determined by the mass of the particle, cf. Eq. (3):

$$\mathrm{FTMS}(\mathbf{x}, t, \tau, r) = \frac{1}{\tau} \ln \left|\left| \frac{\mathrm{d}\phi_t^\tau(\mathbf{x}, r)}{\mathrm{d}r} \right|\right| \tag{6}$$

This scalar field measures the separation of inertial particles that were released from the same location but with slightly different mass. Considering Eq. (5), the field can be equivalently computed from the magnitude of the first derivative of a massline, released at $(\mathbf{x}, t)$, i.e., the massline's stretching:

$$\mathrm{FTMS}(\mathbf{x}, t, \tau, r) = \frac{1}{\tau} \ln \left|\left| \frac{\mathrm{d}\mathbf{m}(r)}{\mathrm{d}r} \right|\right| \tag{7}$$

An example for an FTMS field is given in Fig. 2 for the DOUBLE GYRE [SLM05]. Similar to (inertial) FTLE, FTMS is defined only for particles that do not leave the domain.

At a certain time t, the parameter space of the FTMS scalar field is two-dimensional; it is spanned by response time r and integration duration τ. For an overview, it is interesting to identify for every space-time location, the response time r^* with largest separation, with $r^* \in [r_{\min}, r_{\max}]$:

$$r^* = \arg\max_r \mathrm{FTMS}(\mathbf{x}, t, \tau, r) \tag{8}$$

Fig. 3 shows its corresponding diameter. As an inset in the bottom right corner, we visualize the respective separation:

$$\mathrm{maxFTMS}(\mathbf{x}, t, \tau) = \mathrm{FTMS}(\mathbf{x}, t, \tau, r^*) \tag{9}$$

The response time interval $[r_{\min}, r_{\max}]$ is sampled by a Halton sequence [Hal60] to progressively refine the solution, as shown in the accompanying video. The computation is terminated by the user or after a certain number of iterations. The bounds of the interval are specified by the user as well or might be determined by the underlying equations of motion.

Depicting the maximal separation condenses the information into a visualization that only depends on duration τ, which can be explored by an animation. Of course, this only provides an overview and might not necessarily extract the most interesting separation event. At longer integration time several events might occur and if they exhibit similar separation strength it becomes less clear which to show, see later Section 6.5. For this reasons, maxFTMS cannot replace the detailed inspection of the two-dimensional parameter space. Providing the largest separation at a location, however, serves as a starting point for further investigations. Other separating masses can be observed in the views that are described next.

4. Comparative Visualizations

Once a seed point is found, we investigate the behavior of differently-sized inertial particles released at this location.

4.1. Qualitative View

The mass-dependent flow map $\phi_t^\tau(\mathbf{x}, r)$, as introduced in Section 2.2, has four parameters. Varying one of them and keeping the others constant produces four classes of integral curves [GKKT13]. Among those is the massline from Eq. (5), which connects the locations that were reached by differently-sized inertial particles, i.e., particles with a varying response time r, chosen from an interval $[r_{\min}, r_{\max}]$. Varying two of the parameters similarly produces integral surfaces. In our visualization, we vary the response time r and integration duration τ to depict the temporal evolution of the massline (here, the front line), which forms a *mass-path surface* in space-time as shown in Fig. 4. Thereby, the red and green axes are spatial dimensions and the blue axis is time.

We color-code the particle diameter on the surface and illustrate individual trajectories by an adaptive stripe pattern, as in [HGH*10]. The stripe spacing and the insertion of lines in between them are an indicator for separation. The front line of the surface is a massline (purple). It depicts the location

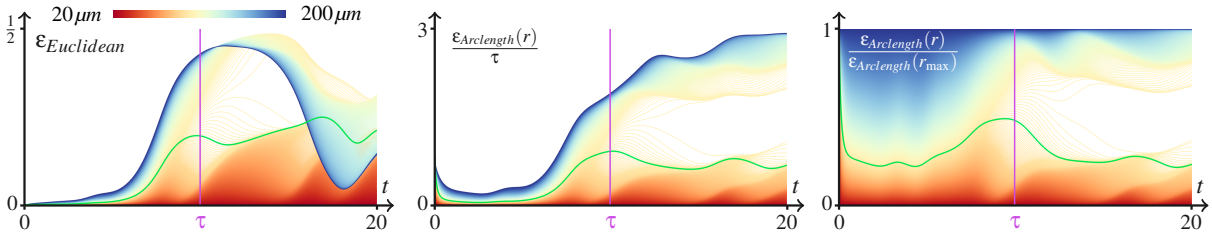

(a) Euclidean distance. (b) Absolute arc length distance. (c) Relative arc length distance.

Figure 5: Distance plots over time in the DOUBLE GYRE, showing the temporal evolution of the difference to the smallest inertial particle ($r = 20\,\mu m$). As in Fig. 4, with selected diameter $d_p = 99\,\mu m$, $\tau = 9.95$ and the seed point $(\mathbf{x}, t) = (0.45417, 0.5675, 0)$.

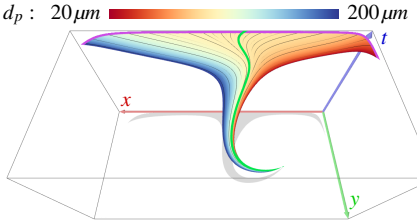

Figure 4: Space-time domain of the DOUBLE GYRE in which inertial particle trajectories form a mass-path surface. The purple line is a massline, the green line depicts the trajectory of the most separating inertial particle, here with $d_p = 99\,\mu m$, $\tau = 9.95$ and seed point $(\mathbf{x}, t) = (0.45417, 0.5675, 0)$.

of inertial particles after the currently selected integration duration. The user can further select a certain particle diameter for closer inspection. We highlight its corresponding particle trajectory by a green line. Color-coding, stripe patterns and highlighting selected lines are all implemented in the pixel shader of the surface. Alternatively, separation on a manifold could be visualized by space-time LIC as in [BSDW12].

4.2. Quantitative View

Another aspect is the mass distribution along a massline. Visualizing its temporal evolution can likewise show separation. Thus, in an additional view, we plot the integration duration τ of inertial particle trajectories vs. a specified distance measure ε, which measures the difference to a reference particle. Again, we color-code trajectories by their diameter. In these plots, a uniform sampling of the response time interval shows separation between the lines by their vertical distance.

Euclidean distance: Bordás et al. [BBK*08, Bor11] measured the distance between experimentally traced particles by Euclidean distance, which was also used to compare experimental and simulated [OOG08] particle positions. Since experiments are conducted with a finite number of differently sized particles, there is no information on the behavior of particles with masses between them. In this paper, we measure the distance to the smallest inertial particle ($r = r_{\min}$):

$$\varepsilon_{Euclidean}(r) = \left|\left|\phi_t^\tau(\mathbf{x}, r) - \phi_t^\tau(\mathbf{x}, r_{\min})\right|\right| \qquad (10)$$

Fig. 5a gives an example for the space-time domain shown in Fig. 4, illustrating the split of particles that hit the domain boundary. While this measure can capture periodicity of events, e.g., recurring proximity, it suffers especially at longer integration times from occlusion and cluttering, which is demonstrated later in Section 6.3.

Arc length distance: To overcome the limitations of the Euclidean distance measure, we propose to measure the arc length of the massline that connects the two particles.

$$\varepsilon_{Arclength}(r) = \int_{r_{\min}}^{r} \left|\left| \frac{\mathrm{d}\mathbf{m}(s)}{\mathrm{d}s} \right|\right| \mathrm{d}s \qquad (11)$$

Such connecting massline exists only iff the particles were seeded at the same location at the same time. In contrast to Euclidean distance, this measure accommodates for the behavior of the masses in between and it monotonically increases with increasing response time, which avoids occlusion since no overlap occurs in the plot. For plotting this measure, we use two different normalizations. We either normalize the error by the integration duration $\frac{\varepsilon_{Arclength}(r)}{\tau}$ to account for the growth of the line over time (as in Fig. 5b), or we use the relative position $\frac{\varepsilon_{Arclength}(r)}{\varepsilon_{Arclength}(r_{\max})}$ to display the evolution of the distribution of masses along the massline (see Fig. 5c).

5. Implementation

Interaction is a crucial aspect in exploration tasks, which requires fast updates on parameter changes. The integration of inertial particles according to Eq. (4), the computation of the mass-path surface in the domain view and the distance plots are all implemented on the GPU, which comfortably achieves interactive frame rates. The maxFTMS field, however, is precomputed, which takes several minutes as listed later in Section 6.4. We discretize the space-time domain of the maxFTMS field onto a regular grid (resolution given in Section 6.4) and progressively sample the mass range. On the GPU, we therefore release inertial particles in the domain and integrate FTMS for the given time interval. In every time slice of the maxFTMS field, we check if the currently considered mass has larger separation than any previously processed mass and store it if this is the case. Finally, the field is stored as a 3D voxel grid (two spatial dimensions and time), with

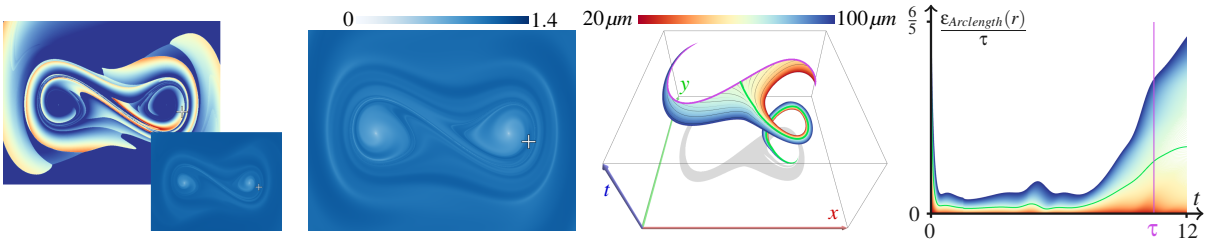

(a) At selected point, $d_p = 64\,\mu m$ has max. separation (maxFTMS). (b) FTMS value for $d_p = 64\,\mu m$ is indeed high. (c) Trajectory with maximal separation on the mass-path surface. (d) Massline arc length-based distance plot to a reference particle.

Figure 6: FORCED DUFFING data set at integration duration $\tau = 10.45$. The seed point is at $(\mathbf{x}, t) = (1.294, -0.22133, 0)$.

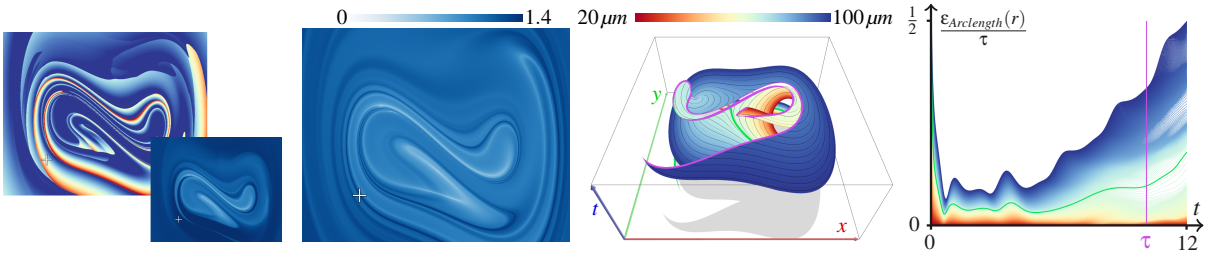

(a) At selected point, $d_p = 69\,\mu m$ has max. separation (maxFTMS). (b) FTMS value for $d_p = 69\,\mu m$ is indeed high. (c) Trajectory with maximal separation on the mass-path surface. (d) Massline arc length-based distance plot to a reference particle.

Figure 7: FORCED-DAMPED DUFFING data at integration duration $\tau = 10.1$ and seed point $(\mathbf{x}, t) = (-1.42613, -1.41141, 0)$.

two entries per cell: the maximal mass and its separation. At runtime, the precomputed maxFTMS and FTMS fields can both be streamed to the GPU for interactive display.

6. Results and Evaluation

We tested our method on a number of analytic and one real-world data set, which are briefly described in the following. In advance, one general note on the units: all domain sizes are assumed to be in meters and time is in seconds.

Double Gyre. The unsteady 2D DOUBLE GYRE [SLM05] became a well-known benchmark data set for the study of particle separation by means of FTLE. We used the form:

$$\mathbf{u}(x, y, t) = \begin{pmatrix} -0.1\pi \sin(f(x,t)\,\pi)\cos(y\pi) \\ 0.1\pi \cos(f(x,t)\,\pi)\sin(y\pi)\,\frac{\mathrm{d}}{\mathrm{d}x} f(x,t) \end{pmatrix} \quad (12)$$

with $f(x,t) = a(t)\,x^2 + b(t)\,x$ and $a(t) = 0.25\sin(t\,\pi/5)$ and $b(t) = 1 - 0.5\sin(t\,\pi/5)$. We consider the domain $D \times T = [0, 0] \times [2, 1] \times [0, 30]$. Examples are shown in Fig. 1 for $\tau = 17$ and throughout Sections 3 and 4 for $\tau = 10$.

Forced Duffing Oscillator. The FORCED DUFFING oscillator in an example for a dynamical system that experiences chaotic behavior [HS11]. It can be described and visualized as an unsteady 2D vector field of the form:

$$\mathbf{u}(x, y, t) = \begin{pmatrix} y \\ x - x^3 + 0.1\sin t \end{pmatrix} \quad (13)$$

here, in the domain $D \times T = [-2, 2]^2 \times [0, 20]$. In Fig. 6a, we show the maxFTMS field and select a seed point. At this seed point, particles with diameter $d_p = 64\,\mu m$ show largest separation. For this diameter, we depict the FTMS field in Fig. 6b. In the space-time domain in Fig. 6c, a mass-path surface is released from the seed point. The trajectory with diameter $d_p = 64\,\mu m$ is highlighted and turns out to run toward a separation point, i.e., a saddle in the inertial dynamics that causes particle separation. The temporal evolution of the massline particles' distance to the smallest inertial particle is shown in Fig. 6d, indicating the separation event as well.

Forced-Damped Duffing Oscillator. A more general form of the oscillator is the FORCED-DAMPED DUFFING oscillator [HS11], which can likewise be described as an unsteady 2D vector field:

$$\mathbf{u}(x, y, t) = \begin{pmatrix} y \\ x - x^3 - 0.25y + 0.4\cos t \end{pmatrix} \quad (14)$$

here, in the domain $D \times T = [-2.5, 2.5]^2 \times [0, 20]$. Fig. 7a depicts the maxFTMS field at $\tau = 10.1$. At the selected point, a particle with diameter $d_p = 69\,\mu m$ shows the largest separation. The corresponding FTMS field is shown for this diameter in Fig. 7b. From the selected point inertial trajectories are released, which assemble in space-time a surface, see Fig. 7c. The trajectory with largest separation is shown on the surface, as well as in the distance plot in Fig. 7d.

Square Cylinder Flow. The SQUARE CYLINDER flow [CSBI05] is a 3D time-dependent flow around an obstacle.

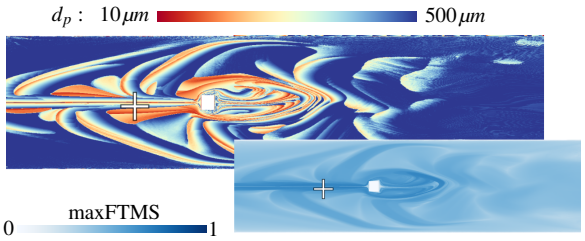

(a) Maximal separation at selection for $d_p = 380\mu m$.

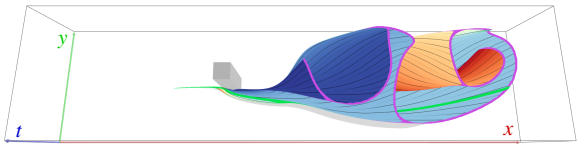

(b) Trajectory with maximal separation on the mass-path surface.

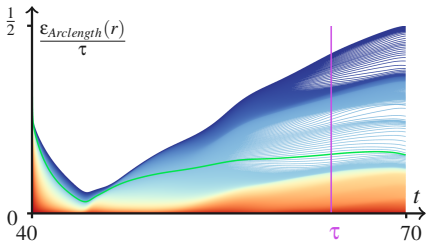

(c) Massline arc length-based distance plot.

Figure 8: SQUARE CYLINDER data set at integration duration $\tau = 64$ and seed point at $(\mathbf{x}, t) = (7.664, 3.77067, 40)$.

It is quite uniform along one dimension, which allows to select one slice and treat it as 2D unsteady flow. As visible in the maxFTMS field in Fig. 8a, large separation occurs for particles that flow toward the obstacle and for particles that enter the vortices of the von Kármán vortex street, since there, rotational movement amplifies the effects of inertia, leading to separation. The latter can be seen by the alternating and periodic separation fronts, running toward and past the obstacle. Selecting one seed point, both space-time domain in Fig. 8b and distance plot in Fig. 8c show multiple separations along the massline. After integration time $\tau = 64$, the strongest arises for a diameter $d_p = 380\mu m$, which is highlighted.

6.1. Comparison between Inertial FTLE and FTMS

Inertial FTLE depicts the separation due to spatial variation of the seed point. The separation due to a varying mass is shown by FTMS. Frequently, both measures have a high correlation, but we observed distinct features that are visible in FTMS only. For instance, in Fig. 9, we see valley lines in FTMS, which do not appear in IFTLE. They may even cross an IFTLE ridge. This means, if a separation of nearby particles occurs, particles with different mass that were released from the same location may still stay together—and, vice versa. In fact, there are two sources of separation to consider: varying mass (FTMS) and variation of the seed point (IFTLE). When

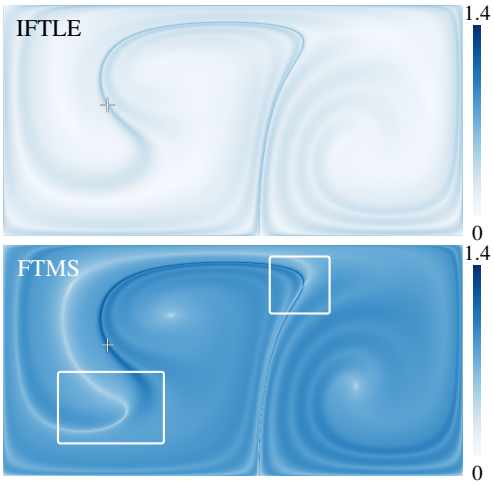

Figure 9: Comparison between inertial FTLE (IFTLE) and FTMS for diameter $d_p = 99\mu m$ at $t = 0$ and $\tau = 9.95$. A corresponding point is selected, showing that ridges in IFTLE and FTMS frequently correlate. However, notice the absence of the white valley lines in IFTLE that even cross ridges.

studying the differences between masses, FTMS is more suitable. Further we found in this example that the separation due to varying mass is stronger, as visible by the color map.

6.2. Low and High Values in FTMS

FTMS depends on the particle response time, which is determined by the particle size. In Fig. 10, we examine this dependence by observing FTMS for different particle sizes at the *same* seed point. For a particle with diameter $d_p = 89.9\mu m$ the seed point has a low FTMS value, i.e., we have low separation. In the space-time domain, this relates to a trajectory that is located in the fold of the mass-path surface. In this data set, this is a place of particularly low separation. In the difference plot, the low separation leads to a strong color gradient. For another diameter $d_p = 73.2\mu m$ the very same seed point has a high FTMS value. In both space-time domain and difference plot the separation becomes apparent, as the selected trajectory runs toward a saddle, causing a separation. As shown by diameter $d_p = 100\mu m$, a high FTMS value does not necessarily relate to saddle-like separation. Similar to FTLE, a difference can also occurs due to shearing. Another example for a saddle-like separation was shown in Fig. 6.

6.3. Comparison between Distance Plots

Section 4.2 introduced two distance measures between differently sized particles: Euclidean distance, Eq. (10), and the arc length of the connecting massline, Eq. (11). In the following, we compare them in more detail at longer integration time. In Fig. 11a, the Euclidean distance between differently-sized inertial particles and the location of a reference particle is shown in the DOUBLE GYRE sequence. In this data set, particles are confined in a closed domain and repeatedly flow

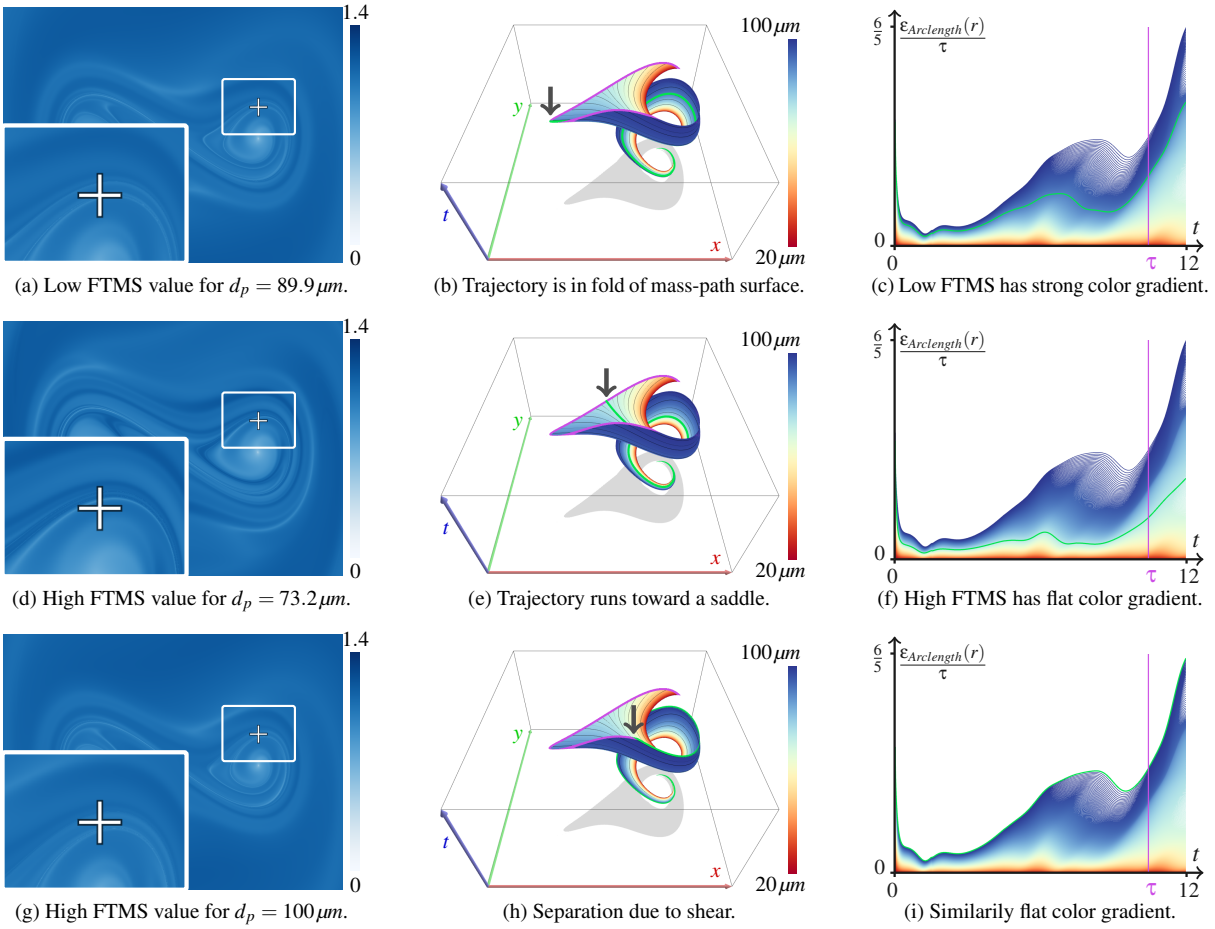

(a) Low FTMS value for $d_p = 89.9\,\mu m$. (b) Trajectory is in fold of mass-path surface. (c) Low FTMS has strong color gradient.

(d) High FTMS value for $d_p = 73.2\,\mu m$. (e) Trajectory runs toward a saddle. (f) High FTMS has flat color gradient.

(g) High FTMS value for $d_p = 100\,\mu m$. (h) Separation due to shear. (i) Similarily flat color gradient.

Figure 10: Comparison of *different* masses that cause small and strong separation, released from the *same* seed point in the FORCED DUFFING data set at integration duration $\tau = 10.45$. The seed point is at $(\mathbf{x}, t) = (1.00496, 0.43565, 0)$.

against a wall, which causes them to split up. These periodic separation events, as well as the recurring particle proximity can be seen in the Euclidean distance plot. However, the longer particles are integrated the more chaotic the distance plot becomes, due to massive occlusion and clutter.

For this reason, we proposed the usage of the arc length distance along the connecting massline to measure the distance to a reference particle, here, the smallest inertial particle. Fig. 11b depicts the temporal evolution of the relative position of a mass along the massline. This plot shows separation events clearer, because occlusion cannot occur. But, as arc length increases over time, separation events become relatively less prominent. At a certain time, multiple masses can experience separation, which is likewise visible.

6.4. Performance

We used an Intel Core i7-2600K CPU with 3.4 GHz and 24 GB RAM, and an Nvidia Quadro K5000 GPU with 4 GB VRAM. The computation time of the maxFTMS field is in the order of minutes and depends on spatial resolution, integration duration and the number of sampled masses. We precompute the sequence on the GPU (see Section 5) and store it to disk. Preprocessing timings of the maxFTMS time series are listed in Table 1. For the DOUBLE GYRE the preprocessing of the full time and mass range took less than two minutes. The FORCED DUFFING had twice the spatial resolution and thus took roughly twice as long. In the FORCED-DAMPED DUFFING, we increased the number of samples in the mass dimension. In our implementation, the sampling of masses is serialized, which linearly increases the number of compute kernel invocations. Thus, with four times more masses, the computation time increases by factor of four. It can further be seen that the smaller temporal resolution had computationally almost no effect. This is because it only reduced the number of max() operations due to fewer time slices. The dominating factor is the fourth-order Runge-Kutta integration of Eq. (4), which was on the same time range for both Duffing oscillators. The time range was given in the data set descriptions in Section 6. The SQUARE CYLINDER flow was the slowest, since

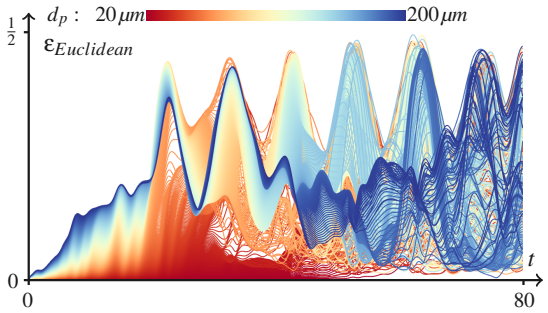

(a) With Euclidean distance periodic events are visible. But, it becomes cluttered with longer integration duration.

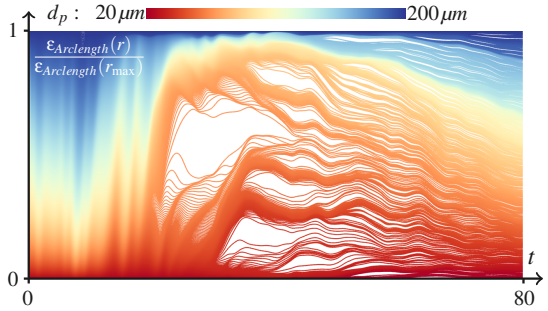

(b) The arc length difference appears more organized and splitting events are better visible.

Figure 11: Periodic events for a long time range in the DOUBLE GYRE: Euclidean (top) clutters eventually. Integration duration τ is in $[0, 80]$, seed point at $(0.83087, 0.28715, 0)$.

Data set	X	Y	T	M	maxFTMS
DOUBLE GYRE	800	400	200	128	1.68
FORCED DUFFING	800	800	200	128	4.75
F-DAMPED DUFFING	800	800	100	512	18.26
SQUARE CYLINDER	800	400	200	256	61.20

Table 1: Space-time resolution of the maxFTMS grid $X \times Y \times T$, number of sampled masses M and the computation time of maxFTMS in minutes.

here flow vector values are sampled from a 3D texture (2D unsteady), rather than being evaluated analytically. In this case, the runtime is bound by fetches from texture memory.

6.5. Limitations

For long integration times, strong separation may occur for multiple masses, as shown in Section 6.3. The maxFTMS field depicts only the mass with strongest separation. If multiple masses have an equally large separation, an effect comparable to z-fighting [AMHH08] occurs, see Fig. 12. The longer the integration, the more likely this artifact becomes.

Also, the mass with maximum separation might not necessarily be the mass that is most interesting, because separation might also happen due to shearing—an artifact known from FTLE. However, while further local maxima of other masses might be hidden behind the global one, our method allows to rule out areas in which no separation occurs at all.

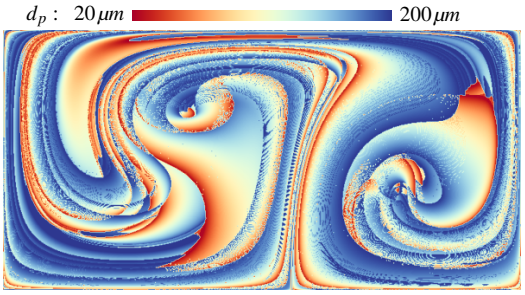

Figure 12: Multiple masses exhibit a similarly strong separation after integration duration $\tau = 30$ in the DOUBLE GYRE.

7. Conclusions and Future Work

In this paper, we presented an approach to a comparative visualization of inertial particle trajectories. For this, we introduced the Finite-Time Mass Separation (FTMS), a scalar field that measures the separation of inertial particles that were released from the same location but with slightly different mass. By extracting for every location in space-time the mass that induced the largest separation, we provided a guiding tool that allows to quickly locate seed points and masses at which differences in inertial particle trajectories can be observed. In additional coordinated views, we displayed inertial particle trajectories at a specified seed point in space-time by integral curves and surfaces. Moreover, we plotted differences to a reference particle over time to observe the mass distribution and the temporal evolution of possibly further separation events.

The next step for future work is the third spatial dimension. Conceptually, the definition of FTMS and the plot view directly carry on into 3D. In the domain view, time cannot be visualized by a spatial axis anymore, which relates to the problem of visualizing path surfaces in 3D, i.e., occlusion and self-intersection become more prominent visualization problems. Also, the depiction of the maxFTMS field needs an extension. It probably reduces to a volume rendering problem, in which two attributes should be shown: the maximum separation and the corresponding mass. In 3D, the computation of the maxFTMS field would be quite expensive. An acceleration of its computation therefore seems a worthwhile topic for future work. Further, the relation with IFTLE deserves more research, possibly including a unified separation measure that accounts for both spatial and mass variation. Another aspect to study is the comparison of trajectories that were computed from different particle models or other equations of motion to see if certain simplifying assumptions can actually be made. Also the comparison of simulated and measured trajectories is an important task. Both require different distance measures, as for those, there are no connecting masslines.

Acknowledgements

The work was partially supported by DFG grant TH 692/8-1.

References

[AMHH08] AKENINE-MÖLLER T., HAINES E., HOFFMAN N.: *Real-Time Rendering 3rd Edition*. A. K. Peters, Ltd., Natick, MA, USA, 2008. 9

[BBC*09] BENZI R., BIFERALE L., CALZAVARINI E., LOHSE D., TOSCHI F.: Velocity-gradient statistics along particle trajectories in turbulent flows: The refined similarity hypothesis in the Lagrangian frame. *Phys. Rev. E 80* (Dec 2009), 066318. 2, 3

[BBC*11] BEC J., BIFERALE L., CENCINI M., LANOTTE A. S., TOSCHI F.: Spatial and velocity statistics of inertial particles in turbulent flows. *Journal of Physics: Conference Series 333*, 1 (2011), 012003. 2

[BBK*08] BORDÁS R., BENDICKS C., KUHN R., WUNDERLICH B., THÉVENIN D., MICHAELIS B.: Coloured tracer particles employed for 3D-PTV in gas flows. In *Proc. International Symposium on Flow Visualization (ISFV)* (July 2008). 5

[BE10] BALACHANDAR S., EATON J. K.: Turbulent dispersed multiphase flow. *Annual Review of Fluid Mechanics 42*, 1 (2010), 111–133. 3

[Bor11] BORDÁS R.: *Optical measurements in disperse two-phase flows: Application to rain formation in cumulus clouds*. PhD thesis, University of Magdeburg, 2011. 1, 2, 5

[BSDW12] BACHTHALER S., SADLO F., DACHSBACHER C., WEISKOPF D.: Space-time visualization of dynamics in Lagrangian coherent structures of time-dependent 2D vector fields. In *Proc. International Conference on Information Visualization Theory and Applications (IVAPP)* (2012), pp. 573–583. 5

[CGP*10] CASCIOLA C. M., GUALTIERI P., PICANO F., SARDINA G., TROIANI G.: Dynamics of inertial particles in free jets. *Physica Scripta 2010*, T142 (2010), 014001. 2

[CSBI05] CAMARRI S., SALVETTI M.-V., BUFFONI M., IOLLO A.: Simulation of the three-dimensional flow around a square cylinder between parallel walls at moderate Reynolds numbers. In *XVII Congresso di Meccanica Teorica ed Applicata* (2005). 6

[CST98] CROWE C., SOMMERFIELD M., TSUJI Y.: *Multiphase Flows with Droplets and Particles*. CRC Press, 1998. 2

[FH15] FARAZMAND M., HALLER G.: The Maxey–Riley equation: Existence, uniqueness and regularity of solutions. *Nonlinear Analysis: Real World Applications 22* (2015), 98–106. 2

[GKKT13] GÜNTHER T., KUHN A., KUTZ B., THEISEL H.: Mass-dependent integral curves in unsteady vector fields. *Comp. Graphics Forum (Proc. EuroVis) 32*, 3 (2013), 211–220. 3, 4

[GT14] GÜNTHER T., THEISEL H.: Vortex cores of inertial particles. *IEEE Trans. on Visualization and Computer Graphics (Proc. IEEE Scientific Visualization) 20*, 12 (2014), 2535–2544. 2, 3

[Hal60] HALTON J.: On the efficiency of certain quasi-random sequences of points in evaluating multi-dimensional integrals. *Numerische Mathematik 2*, 1 (1960), 84–90. 4

[Hal01] HALLER G.: Distinguished material surfaces and coherent structures in three-dimensional fluid flows. *Physica D: Nonlinear Phenomena 149*, 4 (Mar. 2001), 248–277. 2, 3

[HGH*10] HUMMEL M., GARTH C., HAMANN B., HAGEN H., JOY K.: IRIS: Illustrative rendering for integral surfaces. *IEEE Transactions on Visualization and Computer Graphics (Proc. IEEE Scientific Visualization) 16*, 6 (2010), 1319–1328. 4

[HS08] HALLER G., SAPSIS T.: Where do inertial particles go in fluid flows? *Physica D: Nonlinear Phenomena 237* (2008), 573–583. 2, 3

[HS11] HALLER G., SAPSIS T.: Lagrangian coherent structures and the smallest finite-time Lyapunov exponent. *Chaos 21*, 2 (2011), 023115. 6

[KER*14] KUHN A., ENGELKE W., RÖSSL C., HADWIGER M., THEISEL H.: Time line cell tracking for the approximation of Lagrangian coherent structures with subgrid accuracy. *Computer Graphics Forum 33*, 1 (2014), 222–234. 3

[KGRK14] KUTZ B. M., GÜNTHER T., RUMPF A., KUHN A.: Numerical examination of a model rotor in brownout conditions. In *Proceedings of the American Helicopter Society, 70th Annual Forum* (May 2014), no. AHS2014-000343. 1, 2

[KPH*09] KASTEN J., PETZ C., HOTZ I., NOACK B., HEGE. H.-C.: Localized finite-time Lyapunov exponent for unsteady flow analysis. In *Proceedings of Vision, Modeling and Visualization* (2009), pp. 265–274. 3

[KRWT12] KUHN A., RÖSSL C., WEINKAUF T., THEISEL H.: A benchmark for evaluating FTLE computations. In *Proceedings of 5th IEEE Pacific Visualization Symposium (PacificVis 2012)* (Seoul, South-Korea, March 2012), pp. 121–128. 3

[MR83] MAXEY M. R., RILEY J. J.: Equation of motion for a small rigid sphere in a nonuniform flow. *Physics of Fluids 26*, 4 (1983), 883–889. 2

[OOG08] OUELLETTE N. T., O'MALLEY P. J. J., GOLLUB J. P.: Transport of finite-sized particles in chaotic flow. *Phys. Rev. Lett. 101* (2008), 174504. 3, 5

[PD09] PENG J., DABIRI J. O.: Transport of inertial particles by Lagrangian coherent structures: Application to predator–prey interaction in jellyfish feeding. *Journal of Fluid Mechanics 623* (3 2009), 75–84. 1, 2, 3

[PSGC11a] PICANO F., SARDINA G., GUALTIERI P., CASCIOLA C.: DNS of a free turbulent jet laden with small inertial particles. In *Direct and Large-Eddy Simulation VIII*, Kuerten H., Geurts B., Armenio V., Fröhlich J., (Eds.), vol. 15 of *ERCOFTAC Series*. Springer Netherlands, 2011, pp. 189–194. 2, 3

[PSGC11b] PICANO F., SARDINA G., GUALTIERI P., CASCIOLA C. M.: Particle-laden jets: Particle distribution and back-reaction on the flow. *Journal of Physics: Conference Series 318*, 5 (2011), 052018. 3

[RSBE01] ROETTGER S., SCHULZ M., BARTELHEIMER W., ERTL T.: Automotive soiling simulation based on massive particle tracing. In *Data Visualization 2001*, Eurographics. Springer Vienna, 2001, pp. 309–317. 1, 3

[SGL10] SYAL M., GOVINDARAJAN B., LEISHMAN J. G.: Mesoscale sediment tracking methodology to analyze brownout cloud developments. In *Proc. American Helicopter Society, 66th Annual Forum* (2010). 2, 3

[SH08] SAPSIS T., HALLER G.: Instabilities in the dynamics of neutrally buoyant particles. *Phys. Fluids 20* (2008), 017102. 3

[SH09] SAPSIS T., HALLER G.: Inertial particle dynamics in a hurricane. *J. Atmos. Sci. 66* (2009), 2481–2492. 2, 3

[SL99] SHAO Y., LI A.: Numerical modelling of saltation in the atmospheric surface layer. *Boundary-Layer Meteorology 91* (1999), 199–225. 1

[SLM05] SHADDEN S. C., LEKIEN F., MARSDEN J. E.: Definition and properties of Lagrangian coherent structures from finite-time Lyapunov exponents in two-dimensional aperiodic flows. *Physica D: Nonlinear Phenomena 212*, 3–4 (2005), 271–304. 2, 3, 4, 6

[SPH11] SAPSIS T., PENG J., HALLER G.: Instabilities on prey dynamics in jellyfish feeding. *Bull Math Biol. 73*, 8 (2011), 1841–1856. 3

[ÜSE13] ÜFFINGER M., SADLO F., ERTL T.: A time-dependent vector field topology based on streak surfaces. *IEEE Trans. on Visualization and Computer Graphics 19*, 3 (2013), 379–392. 3